Monthly Notices of the ROYAL ASTRONOMICAL SOCIETY

MNRAS **552,** 1–8 (2026) https://doi.org/10.1093/mnras/stag1816
Advance Access publication 2026 September 24
Letter

The mysterious case of iron in XMPs: anomalous high log(Fe/O) observed in extremely metal-poor galaxies HSCJ1631+4426 and SDSSJ0811+4730

Aaron Myszka [1]★ Themiya Nanayakkara [1,2] Karl Glazebrook,[1] Sarah M. Sweet [3] Brent Groves [4,5] Nikole M. Nielsen [1,6] Jarle Brinchmann,[7,8] Yuki Isobe [9,10,11] Chiaki Kobayashi [12] Haruka Kusakabe[13] and Michael V. Maseda [14]

[1]*Centre for Astrophysics and Supercomputing, Swinburne University of Technology, Hawthorn, Victoria 3122, Australia*
[2]*Sydney Institute for Astronomy, School of Physics, The University of Sydney, NSW 2006, Australia*
[3]*School of Mathematics and Physics, University of Queensland, St Lucia, Queensland 4072, Australia*
[4]*International Centre for Radio Astronomy Research, University of Western Australia, 7 Fairway, Crawley 6009 WA, Australia*
[5]*Astronomy Australia Ltd (Perth Office), University of Western Australia, 7 Fairway, Crawley 6009 WA, Australia*
[6]*Homer L. Dodge Department of Physics and Astronomy, The University of Oklahoma, 440 W. Brooks St, Norman, OK 73019, USA*
[7]*Instituto de Astrofisica e Ciências do Espaço, Universidade do Porto, CAUP, Rua das Estrelas, P-4150-762 Porto, Portugal*
[8]*European Southern Observatory, Karl-Schwarzschild-Straße 2, D-85748 Garching, Germany*
[9]*Kavli Institute for Cosmology, University of Cambridge, Madingley Road, Cambridge CB3 0HA, UK*
[10]*Cavendish Laboratory, University of Cambridge, 19 JJ Thomson Avenue, Cambridge CB3 0HE, UK*
[11]*Waseda Research Institute for Science and Engineering, Faculty of Science and Engineering, Waseda University, 3-4-1, Okubo, Shinjuku, Tokyo 169-8555, Japan*
[12]*Centre for Astrophysics Research, Department of Physics, Astronomy and Mathematics, University of Hertfordshire, Hatfield AL109AB, UK*
[13]*Department of General Systems Studies, Graduate School of Arts and Sciences, The University of Tokyo, 3-8-1 Komaba, Meguro-ku, Tokyo 153-8902, Japan*
[14]*Department of Astronomy, University of Wisconsin-Madison, Madison, WI 53706, USA*

Accepted 2026 September 21. Received 2026 August 27; in original form 2026 June 28

ABSTRACT

We present integral field spectroscopic observations of two local extremely metal-poor galaxies (XMPs), HSCJ1631+4426 and SDSSJ0811+4730, obtained with the Keck Cosmic Web Imager (KCWI) over 3545−5529 Å at a spectral resolution of $R \sim 3600$, capturing bright nebular emission lines essential for determining gas-phase metallicity and chemical enrichment measurements. Using integrated spectra, we derive oxygen abundances of $12 + \log(\mathrm{O/H}) = 7.079 \pm 0.010$ and 6.926 ± 0.004, and elevated Fe/O ratios of $\log(\mathrm{Fe/O}) = -1.57 \pm 0.17$ and -1.28 ± 0.07, for HSCJ1631+4426 and SDSSJ0811+4730, respectively. Each galaxy is fully contained within the 8.2 arcsec × 8.0 arcsec field of view, with 0.146 arcsec spaxels providing spatially resolved information. These measurements indicate unusually efficient iron enhancement at extremely low metallicity; Fe/O ratios approach or exceed solar despite oxygen abundances of only ∼2 per cent solar, inconsistent with enrichment from core-collapse supernovae alone or delayed Type Ia supernovae given the young ages of the systems. Comparison with chemical evolution models suggests rare, highly energetic explosions such as bright hypernovae and/or pair-instability supernovae are likely responsible. Our results reinforce the growing evidence that XMPs can reflect the nucleosynthetic processes of early energetic stellar explosions, serving as local laboratories for chemical enrichment pathways prevalent in the early Universe.

Key words: galaxies: abundances – galaxies: evolution – galaxies: fundamental parameters.

1 INTRODUCTION

The study of galaxies in the early stages of chemical enrichment reveals insight into the processes governing star formation, feedback mechanisms, and the impacts of supernovae on the surrounding gas across cosmic time. High α-element abundances (e.g. O, Mg, Si, S, Ar, Ca) indicate enrichment dominated by core-collapse supernovae (CCSNe; K. Nomoto, C. Kobayashi & N. Tominaga 2013), while elevated iron points to Type Ia supernovae (SNe Ia) from lower-mass binary systems (D. Maoz, F. Mannucci & G. Nelemans 2014); the Fe/O ratio can be used to evaluate dominant enrichment mechanisms (C. Kobayashi, A. I. Karakas & H. Umeda 2011; C. C. Steidel et al. 2016; Q.-F. Xing et al. 2019).

★ E-mail: amyszka@swin.edu.au

© The Author(s) 2026.
Published by Oxford University Press on behalf of Royal Astronomical Society. This is an Open Access article distributed under the terms of the Creative Commons Attribution License (https://creativecommons.org/licenses/by/4.0/), which permits unrestricted reuse, distribution, and reproduction in any medium, provided the original work is properly cited.

Downloaded from academic.oup.com/mnras/article/552/3/stag1816/8834024 by :: user on 05 November 2026

Recent *James Webb Space Telescope* (*JWST*)observations have detected elevated nebular Fe/O ratios in high-redshift galaxies (X. Ji et al. 2024; M. Nakane et al. 2024, 2025; S. Tacchella et al. 2025; Y. Isobe et al. 2026), in contrast to iron-deficient, α-enhanced stellar patterns at lower redshift (F. Cullen et al. 2019; D. Kashino et al. 2022; T. M. Stanton et al. 2024), highlighting the need to understand iron enrichment mechanisms across cosmic time. Extremely metal-poor galaxies (XMPs; <10 per cent solar metallicity) in the local Universe serve as accessible analogues to these high-redshift systems (Y. I. Izotov, T. X. Thuan & N. G. Guseva 2012), with strong nebular emission lines and low dust content enabling ideal abundance investigations (Y. I. Izotov et al. 2006; G. Cresci et al. 2010), the latter also reducing the depletion of iron on to dust grains that suppresses gas-phase Fe/O at higher metallicities (J. E. Méndez-Delgado et al. 2024).

Recent studies of XMPs in the local Universe have revealed unexpected chemical abundance patterns that challenge current evolution models and theory. The discovery and analysis of galaxy J0811+4730 by Y. I. Izotov et al. (2018) as well as further works by T. Kojima et al. (2020, 2021) and Y. Isobe et al. (2022) reveal an anomalous large Fe/O ratio for its measure of metallicity. Another such case is found within galaxy J1631+4426, discovered by T. Kojima et al. (2020) and further explored by T. Kojima et al. (2021) and Y. Isobe et al. (2022).

Exhibiting approximately 2 per cent solar metallicity with iron abundance levels comparable to solar, these systems show that high iron-to-oxygen ratios are not supported by any current chemical evolution models. Standard models involving CCSNe and SNe Ia fail to simultaneously produce the enhancement levels of both alpha-elements and iron across the short time-scales experienced by these XMP galaxies (Y. Isobe et al. 2022). This may indicate an influence of additional external enrichment pathways, such as feedback-driven metal redistribution or the accretion of iron-enriched circumgalactic material, though such mechanisms would require fine-tuned conditions to enhance Fe/O without correspondingly elevating the oxygen abundance, and are not supported by current observational evidence (T. Kojima et al. 2021).

Both galaxies are extremely young systems, leaving insufficient time for the delayed iron enrichment from SNe Ia that would typically drive elevated Fe/O at higher metallicities. In young, α-enhanced systems one would instead expect low Fe/O, yet both HSCJ1631+4426 and SDSSJ0811+4730 exhibit the opposite: Fe/O ratios approaching or exceeding solar despite oxygen abundances of only $\sim$2 per cent solar. This inversion requires a non-standard iron source capable of operating on time-scales comparable to massive star evolution.

Other potential sources of these increased iron abundances on short time-scales include theoretical pair-instability supernovae (PISNe) and bright hypernovae (BrHNe). PISNe occur from the explosions of very massive stars ($>$140–300 $M_\odot$; A. Heger & S. E. Woosley 2002), releasing energies of $\sim 10^{53}$ erg, where high-energy photons produce electron-positron pairs, reducing the supportive radiation pressure and triggering an extreme gravitational collapse (G. Rakavy & G. Shaviv 1967; A. Heger & S. E. Woosley 2002). BrHNe are CCSNe from progenitor stars of $\sim 30-100\ M_\odot$ with unusually high explosion energies exceeding 10^{52} erg (M. Modjaz et al. 2020). Each of these events produces large amounts of ^{56}Ni, which rapidly radioactively decays into ^{56}Co and then into ^{56}Fe, a stable isotope which increases the abundance of iron in these systems (H. Umeda & K. Nomoto 2008). Furthermore, both PISNe and BrHNe events occur predominantly in low metallicities (M. Modjaz et al. 2020) as the massive stars required can only be formed in such environments, and neither channel is captured by standard chemical evolution models.

In this letter, we present Keck Cosmic Web Imager (KCWI) observations of galaxies HSCJ1631+4426 and SDSSJ0811+4730, two local XMPs that are among the most metal-poor galaxies known in the local Universe, exhibiting extremely low O/H and anomalously high Fe/O abundances. Previously, analyses involving these objects have relied primarily on single-slit spectroscopy (Y. I. Izotov et al. 2018; T. Kojima et al. 2021; Y. Isobe et al. 2022; T. X. Thuan, N. G. Guseva & Y. I. Izotov 2022), with the exception of Y. Kashiwagi et al. (2021) who presented integral field unit (IFU) observations using the Faint Object Camera and Spectrograph (FOCAS) unit on the Subaru Telescope of HSCJ1631+4426 focused on its oxygen metallicity gradient. Here, we present KCWI IFU spectroscopy of both systems, enabling precise spatial boundary definition and higher signal-to-noise direct-method measurements of both oxygen abundance and iron enrichment. These observations provide crucial constraints on chemical evolution pathways in these objects and, by extension, the low-metallicity early Universe counterparts, indicating a need to revise existing models of stellar feedback and metal enrichment in these primordial galaxies. We adopt the solar metallicity of $12 + \log(\mathrm{O/H}) = 8.69$ and $\log(\mathrm{Fe/O})$ abundance ratio of -1.23 (M. Asplund et al. 2009; M. Asplund, A. M. Amarsi & N. Grevesse 2021).

2 OBSERVATIONS AND DATA PROCESSING

The observations of the two XMPs HSCJ1631+4426 ($z = 0.031$) and SDSSJ0811+4730 ($z = 0.044$) were obtained with the KCWI on the Keck II telescope on the 2022 March 25. All exposures were taken using the small slicer IFU with the BL grating, covering the wavelength range 3545−5529 Å at a spectral resolution of $R \sim 3600$, under seeing conditions of approximately 0.9 arcsec for SDSSJ0811+4730 and 0.85 arcsec for HSCJ1631+4426. Between sets of exposures, 90° rotations were applied to improve spatial sampling, allowing the rectangular IFU spaxels to be effectively reconstructed as square spatial elements in the final data cubes. A total of six 1800-s exposures were taken for SDSSJ0811+4730 and eight 1800-s exposures for HSCJ1631+4426, corresponding to total integration times of 3 and 4 h, respectively. The two galaxies in their observed field of view (FOV) are shown in Fig. 1(a).

The data were reduced and exposures combined following the methods outlined in N. M. Nielsen et al. (2022). We used the IDL version of the KCWI Data Reduction Pipeline (DRP; v1.2.2)[1] with standard settings where we skipped the sky subtraction step (`kcwi_stage5sky`), with flux calibrations done with standard star feige56 from the KCWI DRP starlist. We further reduced the data using in-house software (N. M. Nielsen et al. 2022) to remove a residual 10 per cent illumination gradient across the FOV, producing final data cubes that are flux-calibrated, sky-subtracted using in-frame skies, and flat to within 1 per cent. We used `Montage`[2] to optimally combine all exposures for a given galaxy, reproject the data on to square spaxels, and crop the data to the region over which all exposures overlap, resulting in final data cubes of 8.2 arcsec × 8.0 arcsec with 0.146 arcsec spaxels. The

[1] https://github.com/Keck-DataReductionPipelines/KcwiDRP
[2] http://montage.ipac.caltech.edu/

Downloaded from academic.oup.com/mnras/article/552/3/stag1816/8834024 by :: user on 05 November 2026

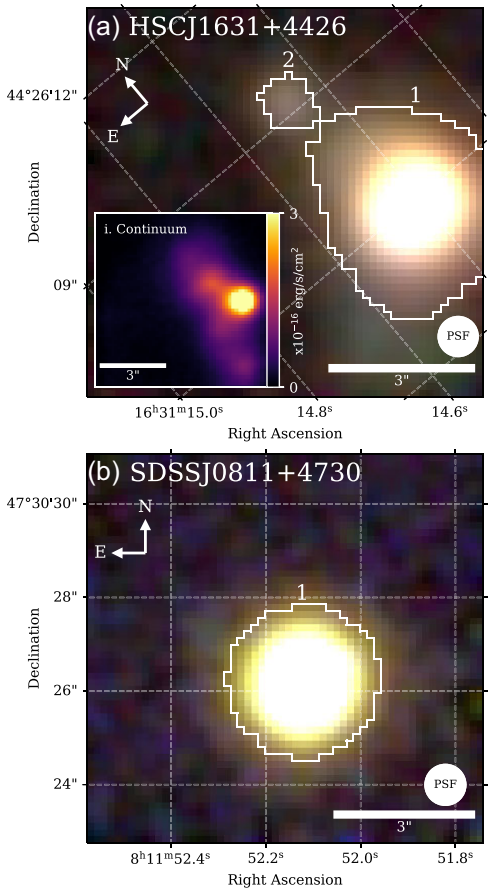


Figure 1. Composite RGB images of (a) HSCJ1631+4426 and (b) SDSSJ0811+4730. Each image is constructed from the fitted line fluxes of [O III] λ5007 (red), Hβ (green), and the combined [O II] λ3726 + λ3729 doublet (blue). Galaxy boundaries identified using `astrodendro` are overlaid in white, with the individual boundaries numbered for reference. A PSF circle and 3-arcsec scale bar are shown bottom right. An inset is included towards the lower left of panel a to display the map of the summed fitted continuum of this galaxy; such extended features are not present for SDSSJ0811+4730.

datacubes were then continuum-subtracted using the `fit_spec` function of the PYPLATEFIT package by R. Bacon et al. (2023).

Once the nebular emission was isolated, emission lines of each spectrum in each spaxel was fitted using the routine outlined within A. Myszka et al. (2025), based on the LMFIT package by M. Newville et al. (2014). Due to continuing difficulties with reported uncertainties within LMFIT (covered in A. Myszka et al. 2025), we again determined line flux uncertainties through a per-spectra RMS-based approach. We note that this approach does not account for Poisson noise in bright emission lines such as Hβ and [O III] λ5007, and as such their uncertainties are likely underestimated. However, as the faint iron lines driving our abundance measurements are dominated by continuum noise, we do not expect this to impact our derived log(Fe/O) values or Monte Carlo uncertainties.

Through the initial inspection of the datacubes, it became apparent that the data for HSCJ1631+4426 included an interesting feature. Along with the primary body of the galaxy, there are also diffuse features extending out from the body in two directions, one towards the north and the other more south-east. These features are comparably quite subtle, so they can only be faintly seen in Fig. 1.

To distinguish between these features and construct integration boundaries, the ASTRODENDRO PYTHON package by T. Robitaille et al. (2019) was used on the summed Hβ and [O III] λ5007 flux maps. Boundaries were determined by a global noise-map RMS threshold, feature contrast, and point spread function (PSF) size criteria. The resulting boundaries, including one around the brighter northern prominence of HSCJ1631+4426, are indicated in Fig. 1. The northern prominence is blueshifted by $\boldsymbol{\Delta v \approx 22}$ km s^{-1} relative to the primary body, as measured from the fitted [O III] λ5007 centroids of the two integrated spectra.

In conjunction with the spatially resolved data set, results using the fully integrated spectra of the two galaxies were also produced. To integrate the three bounded sections independently, spectra were combined by weighting each spaxel by its fitted [O III] λ5007 flux before summation. This gives greater weight to spaxels of higher line flux, maximizing the signal-to-noise of the resulting integrated spectrum relative to a uniform sum over the boundary. The integrated spectra were then taken through an identical continuum fitting and subtraction process as outlined above, and then the same emission line fitting process. The final processed spectra can be seen in Fig. 2.

Prior to abundance analysis, integrated line fluxes were corrected for dust attenuation by fitting $E(B-V)$ via least-squares minimization over the 21 available Balmer lines from Hγ to Hω measured relative to Hβ against theoretical Case B values (D. E. Osterbrock 1989), applying the J. A. Cardelli, G. C. Clayton & J. S. Mathis (1989) extinction law. Hζ λ3889 was excluded here due to blending with He I λ3888.6. We obtain $E(B-V) = 0.014 \pm 0.003$ for HSCJ1631+4426 and $E(B-V) = -0.084 \pm 0.001$ for SDSSJ0811+4730; the negative value for SDSSJ0811+4730 is clipped to zero, consistent with the negligible dust content expected at such low metallicity. The resulting corrections are small ($\lesssim$7 per cent) as expected for XMP galaxies. The fitted and dereddened flux values of these emission lines are shown in Table 1.

3 RESULTS

We measure elemental abundances through the use of the PYNEB PYTHON package by V. Luridiana, C. Morisset & R. A. Shaw (2015, v1.1.22), adopting a two-zone temperature scheme with separate electron temperatures for the O^+ and O^{2+} ionization zones. We first evaluate density and [O III] electron temperature iteratively through the use of the `getTemDen` procedure, using [O II] F(λ3726)/F(λ3729) as the density line ratio and [O III] F(λ4959 + λ5007)/F(λ4363) as the temperature ratio. The initial temperature is set to 10^4 K, and the initial density is set to 100 cm^{-3}; these quickly converge to the reported values within a small number of iterations (<5). The [O II] temperature is then evaluated using the empirical T_e ([O II]) = 0.7 T_e ([O III]) + 3000 K, as verified by A. Campbell, R. Terlevich & J. Melnick (1986) and D. R. Garnett (1992).

The ionic abundances of O^+ and O^{2+} are then calculated using the `getIonAbundance` procedure within PYNEB. The O^+ abundance was determined using the combined [O II] λλ3726, 9 flux relative to the Hβ flux, while the O^{2+} abundance used the relative [O III] λ4959 + λ5007 flux. These abundance values are then combined under the assumption $O/H = O^+/H^+ + O^{2+}/H^+$ to calculate the final oxygen abundance.

Measurements within the second boundary of HSCJ1631+4426 could not be reliably determined because

Downloaded from academic.oup.com/mnras/article/552/3/stag1816/8834024 by :: user on 05 November 2026

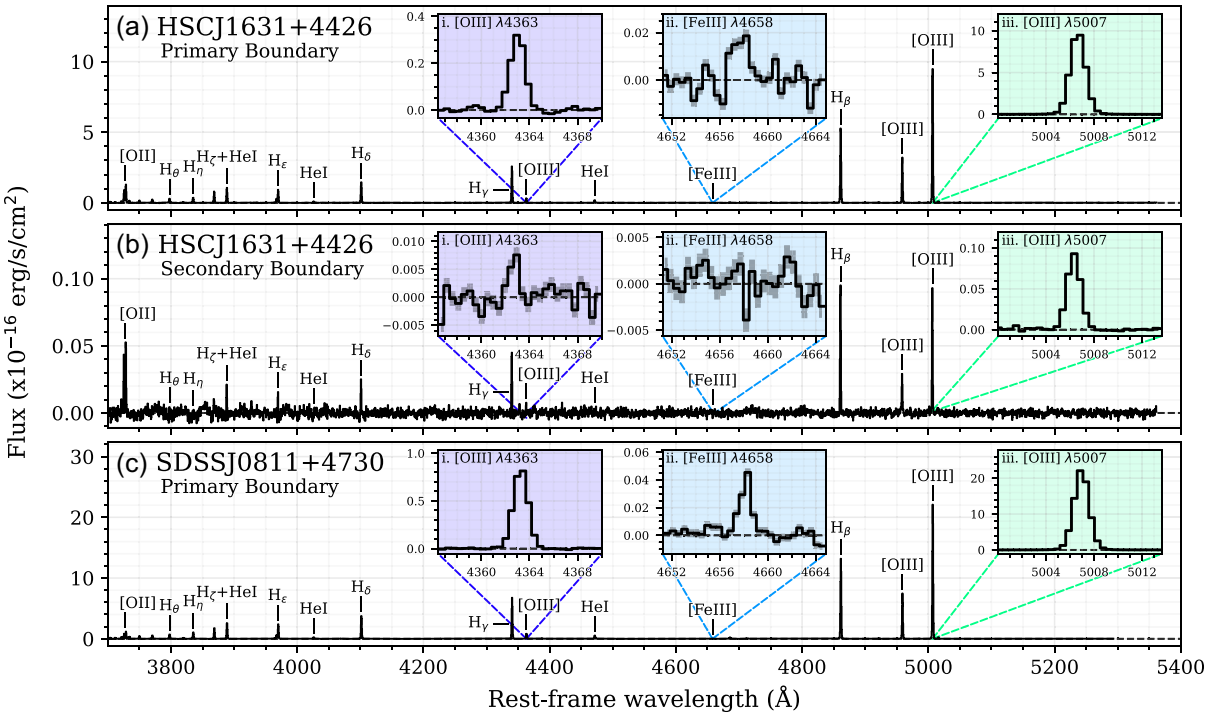


Figure 2. The rest-frame integrated spectra of (a) the primary boundary of HSCJ1631+4426, (b) the secondary boundary of HSCJ1631+4426, and (c) SDSSJ0811+4730. Spectra are extracted within boundaries shown in Fig. 1, continuum-subtracted. Within each panel, insets are provided to show a more detailed view of the spectra around the positions of (i) [O III] λ4363, (ii) [Fe III] λ4658, and (iii) [O III] λ5007. 1σ intervals are shown shaded in grey.

the required emission lines were unable to be detected in its integrated spectrum. Therefore, this region is excluded from the study. Results from the primary boundary of this galaxy are hereafter referred to simply as HSCJ1631+4426.

We determine the metallicity within HSCJ1631+4426 to be $12 + \log(\mathrm{O/H}) = 7.079 \pm 0.010$ and that of SDSSJ0811+4730 to be $12 + \log(\mathrm{O/H}) = 6.926 \pm 0.004$, broadly consistent with, though not within 1σ of, previous literature values of 6.90 ± 0.03 (T. Kojima et al. 2020) and 6.98 ± 0.02 (Y. I. Izotov et al. 2018), respectively.

The ionic abundance of Fe^{2+} is similarly determined using the `getIonAbundance` procedure, using the measured [Fe III] λ4658 flux relative to Hβ. A value for the total iron abundance is then obtained through the `getElemAbundance` step, taking the O^+ and O^{2+} abundances in conjunction with the low-metallicity ionization correction factor (ICF) of Y. I. Izotov et al. (2006).

Through this method, we obtain a value of $\log(\mathrm{Fe/O}) = -1.57 \pm 0.17$ for HSCJ1631+4426 and a value of $\log(\mathrm{Fe/O}) = -1.28 \pm 0.07$ for SDSSJ0811+4730, consistent with but significantly more precise than previous measurements of $-1.25^{+0.17}_{-(0.31+0.22)}$ and $-1.06^{+0.09}_{-(0.09+0.22)}$ (T. Kojima et al. 2021), reflecting our more secure [Fe III] λ4658 detections.

The uncertainties on the metallicity and iron enrichment values are determined by performing 1000 Monte Carlo iterations, altering line flux measurements by sampling a normal distribution of standard deviation equal to the respective line flux uncertainties each time.

We also determine elemental abundances adopting a second ionization correction model, that of M. Rodríguez & R. H. Rubin (2005). This model applies a different ionization correction scheme, and has been shown to produce values approximately 0.2 dex lower (T. Kojima et al. 2021; Y. Isobe et al. 2022). Through this process, we find iron enrichments of -1.80 ± 0.16 for HSCJ1631+4426 and -1.55 ± 0.08 for SDSSJ0811+4730, corresponding to decreases in $\log(\mathrm{Fe/O})$ of 0.23 and 0.27, respectively, in agreement with previous literature. These differences are treated as additional systematic uncertainties and discussed further in Section 4.

We also test the sensitivity of the derived $\log(\mathrm{Fe/O})$ to the choice of [Fe III] atomic data by repeating the abundance calculation across all six data sets available in PYNEB,[3] finding that the derived values range from −1.62 to −1.52 (0.10 dex) for HSCJ1631+4426 and −1.35 to −1.22 (0.13 dex) for SDSSJ0811+4730, with the adopted default data set sitting near the centre of each distribution.

Integrated $12 + \log(\mathrm{O/H})$ metallicity and $\log(\mathrm{Fe/O})$ iron enrichment values are shown, together with the derived intermediate quantities and additional sources of uncertainty, in Table 2.

If we neglect to separate the extended features from the primary structure of HSCJ1631+4426, combining the light from across the whole FOV, we approach near identical metallicity and iron enrichment values of $12 + \log(\mathrm{O/H}) = 7.08 \pm 0.02$ and $\log(\mathrm{Fe/O}) = -1.57 \pm 0.19$. This indicates that any differences to the line ratios and abundances within the extended features of this galaxy are completely dominated by the bright emissions

[3]The six [Fe III] atomic data sets available in PYNEB v1.1.22 are from N. R. Badnell & C. P. Ballance (2014) (144 levels, default), N. R. Badnell & C. P. Ballance (2014) (34 levels), N. C. Deb & A. Hibbert (2009), S. N. Nahar & A. K. Pradhan (1996), P. Quinet (1996), and P. Quinet (1996) combined with S. Johansson et al. (2000), all revised by C. Mendoza et al. (2023).

Downloaded from academic.oup.com/mnras/article/552/3/stag1816/8834024 by :: user on 05 November 2026

Table 1. Fitted and de-reddened flux values for key and supplementary emission lines measured in the integrated spectra of the two XMP galaxies. Wavelengths are given as measured in air. Fluxes are shown normalized to F(Hβ) = 100. Lines of signal-to-noise ratio less than the threshold of 3 (undetected) are given as upper limits. Measured line fluxes from the same spectrum (boundary) hold the same uncertainty values due to the RMS-based approach mentioned in Section 2. The [Fe II] line marked with a star ($\star$) is likely blended with permitted Fe II emission; non-detection of [Fe II] λ4244 suggests the forbidden contribution is negligible.

		HSCJ1631+4426		SDSSJ0811+4730
Line	λ (Å)	Boundary 1	Boundary 2	Boundary 1
[O II]	3726.032	15.35 ± 0.11	51.06 ± 2.58	5.91 ± 0.04
[O II]	3728.815	22.42 ± 0.11	68.86 ± 2.58	7.90 ± 0.04
He I	3819.6074	0.88 ± 0.11	<7.74	0.96 ± 0.04
[Ne III]	3868.760	14.00 ± 0.11	11.55 ± 2.58	12.87 ± 0.04
He I	3888.648	13.88 ± 0.11	18.44 ± 2.58	14.53 ± 0.04
He I	3964.7291	0.77 ± 0.11	<7.74	0.80 ± 0.04
[Ne III]	3967.470	5.09 ± 0.11	<7.74	4.55 ± 0.04
Hϵ	3970.079	16.19 ± 0.11	14.28 ± 2.58	17.04 ± 0.04
He I	4026.190	1.65 ± 0.11	<7.74	1.88 ± 0.04
Hδ	4101.742	26.00 ± 0.11	24.98 ± 2.58	27.29 ± 0.04
He I	4143.761	< 0.33	<7.74	0.31 ± 0.04
Hγ	4340.471	46.83 ± 0.11	50.47 ± 2.58	49.65 ± 0.04
[Fe II] *	4358.162	< 0.33	<7.74	0.15 ± 0.04
[O III]	4363.210	5.63 ± 0.11	<7.74	6.10 ± 0.04
He I	4387.929	0.37 ± 0.11	<7.74	0.47 ± 0.04
He I	4471.479	3.45 ± 0.11	<7.74	3.96 ± 0.04
[Fe III]	4658.050	0.34 ± 0.11	<7.74	0.27 ± 0.04
He II	4685.710	0.72 ± 0.11	<7.74	1.83 ± 0.04
[Ar IV]	4711.260	0.35 ± 0.11	<7.74	0.38 ± 0.04
He I	4713.1457	0.46 ± 0.11	<7.74	0.64 ± 0.04
[Ar IV]	4740.120	< 0.33	<7.74	0.31 ± 0.04
Hβ	4861.333	100.00 ± 0.11	100.00 ± 2.58	100.00 ± 0.04
He I	4921.9313	0.87 ± 0.11	<7.74	0.91 ± 0.04
[O III]	4958.911	56.96 ± 0.11	27.76 ± 2.58	54.21 ± 0.04
[Fe I]	4985.9838	0.66 ± 0.11	<7.74	0.31 ± 0.04
[O III]	5006.843	171.98 ± 0.11	87.27 ± 2.58	162.23 ± 0.04
He I	5015.6783	1.76 ± 0.11	<7.74	1.81 ± 0.04
F(Hβ), 10^{-16} erg s^{-1} cm^{-2}	9.941 ± 0.010	0.285 ± 0.007	22.849 ± 0.010	

contained within its primary boundary and are therefore unmeasurable in the data.

We measure the equivalent width of Hβ, EW$_0$(Hβ), from the continuum fit in spectral windows either side of the Hβ line (4825–4845 Å and 4880–4900 Å), obtaining 121.9 ± 0.6 Å and 271.3 ± 1.3 Å for HSCJ1631+4426 and SDSSJ0811+4730, respectively.

4 DISCUSSION

The derived oxygen abundances confirm that both HSCJ1631+4426 and SDSSJ0811+4730 are among the most chemically pristine star-forming galaxies in the known local Universe; both fall significantly below 10 per cent Z$_\odot$ to be classed as XMPs. Coupled with the elevated Fe/O ratios measured in both systems, this strongly suggests a non-standard enrichment pathway not captured by conventional chemical evolution models.

The contributions of SNe Ia drive an increase in log(Fe/O) at metallicities of 12 + log(O/H) > 8 (T. Bensby & S. Feltzing 2006), with the accumulation of iron below this threshold owing primarily to CCSNe (T. Kojima et al. 2021). When compared to Galactic stellar abundances, the two galaxies exhibit a clear divergence

Table 2. Integrated properties of the primary boundary of HSCJ1631+4426 and SDSSJ0811+4730. The properties of the secondary boundary of HSCJ1631+4426 are not given as none were measurable. Reported uncertainties on log(Fe/O) reflect Monte Carlo propagation of line flux uncertainties only. $\Delta\log(\mathrm{Fe/O})_{\mathrm{ICF}}$ and $\Delta\log(\mathrm{Fe/O})_{\mathrm{atom}}$ give the additional systematic offsets from the choice of ionization correction factor and [Fe III] atomic data, respectively, as discussed in Section 4.

Property	HSCJ1631+4426	SDSSJ0811+4730
EW$_0$(Hβ)	121.9 ± 0.6	271.3 ± 1.3
T_e([O III]), K	19 729 ± 221	21 522 ± 107
T_e([O II]), K	16 810 ± 155	18 066 ± 75
n$_e$, cm^{-3}	17.63 ± 9.08	129.64 ± 13.00
$O^+/H^+(\times10^{-6})$	2.19 ± 0.06	0.674 ± 0.008
$O^{2+}/H^+(\times10^{-6})$	9.80 ± 0.23	7.75 ± 0.08
O/H ($\times10^{-5}$)	1.20 ± 0.03	0.843 ± 0.008
12 + log(O/H)	7.079 ± 0.010	6.926 ± 0.004
$Fe^{2+}/H^+(\times10^{-8})$	4.29 ± 1.36	2.56 ± 0.42
Fe/H ($\times10^{-7}$)	3.19 ± 1.01	4.40 ± 0.73
log(Fe/O)	−1.57 ± 0.17	−1.28 ± 0.07
$\Delta\log(\mathrm{Fe/O})_{\mathrm{ICF}}$	−0.23	−0.27
$\Delta\log(\mathrm{Fe/O})_{\mathrm{atom}}$	±0.10	±0.13

Downloaded from academic.oup.com/mnras/article/552/3/stag1816/8834024 by :: user on 05 November 2026

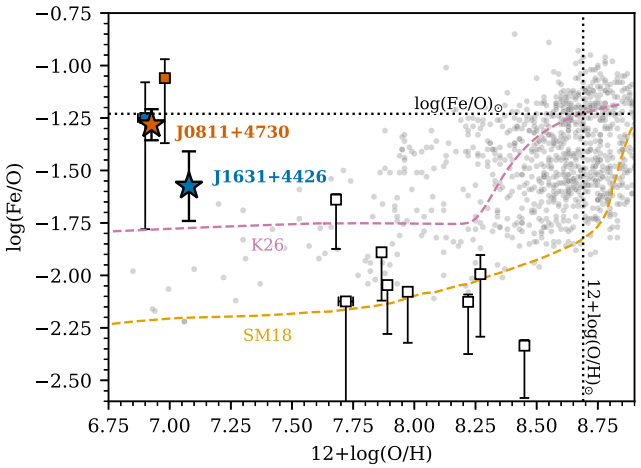


Figure 3. A comparison of Fe/O and 12 + log(O/H) data, adapted from T. Kojima et al. (2021), with our results for the primary boundary of HSCJ1631+4426 and SDSSJ0811+4730 shown as coloured stars. Error bars on the star symbols indicate Monte Carlo uncertainties; systematic uncertainties from the ICF and [Fe III] atomic data choices are discussed in Section 3. Galaxies from the T. Kojima et al. (2021) sample are shown as square points, with HSCJ1631+4426 and SDSSJ0811+4730 in their respective colours; stellar data from T. Bensby, S. Feltzing & M. S. Oey (2014), R. Cayrel et al. (2004), R. G. Gratton et al. (2003), B. Edvardsson et al. (1993), and B. E. Reddy et al. (2003) are shown as circles. Dashed lines show the Milky Way chemical evolution models of A. Suzuki & K. Maeda (2018) (9−100 $M_\odot$ gas enrichment) and a new model computed for this work (K26), extending C. Kobayashi, A. I. Karakas & M. Lugaro (2020) with a flattened Population III IMF (10−280 $M_\odot$, $x = 0$ versus standard Salpeter $x = 1.35$) to enable PISNe. Uncertainties in 12 + log(O/H) are too small to be seen under point markers; see Table 2.

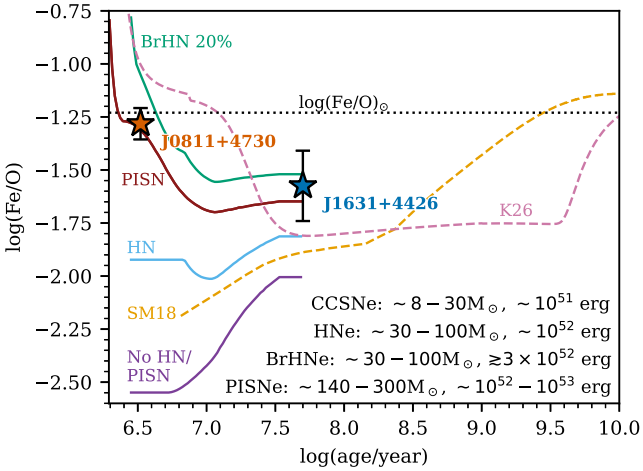


Figure 4. Fe/O-age evolutionary tracks, adapted from Y. Isobe et al. (2022), with our results for HSCJ1631+4426 and SDSSJ0811+4730 overlaid. Solid lines indicate theoretical chemical evolution model pathways (Y. Isobe et al. 2022) for a 20 per cent proportion of bright hypernovae (BrHN 20 per cent), pair-instability supernovae (PISN), entirely hypernovae (HN), or no hypernovae/PISNe (No HN/PISN). Dashed lines show the Milky Way Fe/O models of A. Suzuki & K. Maeda (2018) (9−100 $M_\odot$ gas enrichment) and a new model computed for this work (K26), extending C. Kobayashi et al. (2020) with a flattened Population III IMF (10−280 $M_\odot$, $x = 0$ versus standard Salpeter $x = 1.35$) to enable PISNe. Error bars indicate Monte Carlo uncertainties; ICF and [Fe III] atomic data systematics are discussed in Section 3. The solar log(Fe/O) is shown as the horizontal dotted line. Progenitor mass and explosion-energy ranges from A. Heger & S. E. Woosley (2002) and Y. Isobe et al. (2022); HNe and BrHNe share similar progenitor mass ranges but differ in explosion energy, with BrHNe representing the higher-energy subset.

from the Milky Way Fe/O evolutionary track, being well below 12 + log(O/H) = 8 with very high log(Fe/O).

Fig. 3 shows the positions of the two XMP galaxies in metallicity-log(Fe/O) space, highlighting their anomalously high iron enrichment.

T. Kojima et al. (2021) investigate whether the elevated log(Fe/O) ratios could be artificially inflated by hard extreme-ultraviolet radiation, shock heating, or contamination from C IV λ4659, and rule out each of these effects as a dominant contributor. The authors also find that the preferential depletion of iron into dust relative to oxygen dominates as metallicity increases, producing the negative correlation between log(Fe/O) and 12 + log(O/H) visible in the T. Kojima et al. (2021) sample in Fig. 3 (square points). However, such dust formation is negligible at the extremely low metallicities of HSCJ1631+4426 and SDSSJ0811+4730; this effect cannot explain their elevated iron enhancements.

Y. Isobe et al. (2022) additionally exclude the contributions of SNe Ia to the iron enrichment of SDSSJ0811+4730, due to its approximate age of only ∼10 Myr, as well as indicating HSCJ1631+4426 cannot be consistent with the MW model to 1σ. Their measurements of the N/O ratio for each galaxy also support their conclusions. Based on these constraints, the authors identify enrichment from BrHNe and/or PISNe as the most plausible mechanisms for producing the elevated iron enrichment. We note that the previous [Fe III] λ4658 detection in HSCJ1631+4426 was marginal at 2.4σ (T. Kojima et al. 2021); our KCWI data improve this to 3.1σ and 6.8σ for HSCJ1631+4426 and SDSSJ0811+4730, respectively, lending greater confidence to the derived Fe/O values.

Fig. 4 displays several Fe/O-age evolutionary tracks with the positions of the two XMP galaxies overlaid. Here, we combine the iron enrichment values determined through this work with the 50 Myr age of HSCJ1631+4426 reported by T. Kojima et al. (2020) and the age of SDSSJ0811+4730 by Y. I. Izotov et al. (2018) of 3.3 Myr. This comparison indicates that for such elevated iron enrichment to occur, current models predict that contributions from the highly energetic BrHNe and/or PISNe are required at the young ages of these systems. Independent $EW_0(H\beta)$ age estimates from PYSTARBURST99 (C. Hawcroft et al. 2025) yield ∼4.1 Myr for HSCJ1631+4426 and ∼2.8 Myr for SDSSJ0811+4730, significantly younger than the ∼50 Myr of T. Kojima et al. (2020) derived via SED fitting, likely reflecting the greater sensitivity of the EW method to the current starburst rather than the integrated stellar population. Regardless of which estimate is adopted, both ages are well below the ∼1 Gyr delay time for significant SNe Ia iron enrichment (D. Maoz et al. 2014), reinforcing that the observed Fe/O excess cannot be attributed to delayed iron production.

We note that both galaxies have stellar masses of $\log(M_\star/M_\odot) \lesssim 6.3$ (Y. I. Izotov et al. 2018; T. Kojima et al. 2020), raising the question of whether the high-mass stellar tail of the IMF is sufficiently populated to produce PISNe or BrHNe in a statistical sense. Scaling the PYSTARBURST99 ionizing output to the observed Hβ luminosities of 2.2×10^{39} and 1.0×10^{40} erg s^{-1} for HSCJ1631+4426 and SDSSJ0811+4730, respectively, implies burst masses of ∼2 and ∼ 5×10^5 $M_\odot$, sufficient for

Downloaded from academic.oup.com/mnras/article/552/3/stag1816/8834024 by :: user on 05 November 2026

a G. Chabrier (2003) initial mass function (IMF) to populate the very massive tail with tens of stars above 140 $M_\odot$ such that enrichment need not rely on a single statistical fluctuation.

The same luminosities, combined with our measured T_e and n_e, imply $\sim 10^6\,M_\odot$ of ionized gas and hence only $\sim$25–30 $M_\odot$ of iron in the emitting phase. This is a lower limit, as neither neutral gas nor iron depleted on to dust is accounted for. Since a single PISN can synthesize tens of $M_\odot$ of ^{56}Ni (A. Heger & S. E. Woosley 2002), and even a normal hypernova $\sim$0.4 $M_\odot$ of iron (Y. Isobe et al. 2022), the observed enrichment requires only a small number of such events rather than a finely tuned population, well within the population implied by the burst masses above. Therefore, the proposed scenario is consistent with the absolute emission-line luminosities as well as the abundance ratios.

While the results favour enrichment pathways involving PISNe and/or BrHNe, we emphasize that iron abundance measurements in XMPs carry substantial systematic uncertainty that the literature has yet to fully resolve. The dominant sources are the choice of ionization correction factor, which alone introduces a systematic uncertainty of $\sim 0.2-0.3$ dex seen in this study and the previous by Y. Isobe et al. (2022), the choice of [Fe III] atomic data, which contributes a further $\sim 0.10-0.13$ dex as quantified in Section 3, and the reliance on a single [Fe III] emission line. We also note that the Y. I. Izotov et al. (2006) ICF was calibrated under standard star-forming conditions, and harder ionizing radiation in these systems could in principle affect the iron ICF more than other abundance ratios; however, comparing the ionization parameter proxy [O III]/[O II] against log(Fe/O) across our sample and the broader XMP sample of T. Kojima et al. (2021) reveals no significant correlation (Spearman $\rho = 0.17$, $p = 0.61$), suggesting this is not the dominant driver. Despite these uncertainties, the persistence of elevated log(Fe/O) across multiple independent studies, ionization models, and observational data sets demonstrates that the conclusion of anomalously efficient iron production at extremely low metallicity is robust. Firmly establishing the enrichment mechanism will ultimately require both improved atomic data for Fe^{2+} and observations of additional abundance diagnostics.

In a sample of local XMPs, K. Watanabe et al. (2024) demonstrates that Ar/O and S/O ratios fall well below the predictions of PISN chemical evolution models, favouring enrichment by CCSNe/HNe with mixing and fallback over PISNe, despite those same galaxies exhibiting elevated Fe/O. Future red-optical observations extending to the [Ar III] λ7136 and [S II]/[S III] lines in HSCJ1631+4426 and SDSSJ0811+4730 would therefore be valuable for determining whether PISNe are truly required to explain the observed iron enrichment, or whether BrHNe alone can suffice.

5 SUMMARY AND CONCLUSIONS

We present spatially resolved KCWI spectroscopy of the extremely metal-poor galaxies HSCJ1631+4426 and SDSSJ0811+4730 ($Z < 2.5$ per cent $Z_\odot$), which exhibit unusually high iron enrichment relative to oxygen despite their chemically primitive nature. Integrating the KCWI spectra within well-defined spatial boundaries, we measure over 40 nebular emission lines to derive electron temperatures, densities, and gas-phase abundances, obtaining $12 + \log(O/H) = 7.079 \pm 0.010$ and $\log(Fe/O) = -1.57 \pm 0.17$ for HSCJ1631+4426, and $12 + \log(O/H) = 6.926 \pm 0.004$ and $\log(Fe/O) = -1.28 \pm 0.07$ for SDSSJ0811+4730.

Despite their extremely low oxygen abundances, both galaxies display Fe/O ratios comparable to Milky Way stars at much higher metallicities, inconsistent with standard CCSNe yields or delayed SNe Ia enrichment given their young ages; comparison with chemical evolution models instead requires contributions from rare, highly energetic explosions such as PISNe and/or BrHNe.

While iron abundances are sensitive to the choice of ionization correction and [Fe III] atomic data, the persistence of elevated Fe/O across multiple studies and data sets confirms the conclusion of unusually efficient iron production at extremely low metallicity is robust; the derived abundances are dominated by the brightest emission, with no measurable contribution from lower-surface-brightness extended features.

These results strengthen the growing evidence that early chemical enrichment in extremely metal-poor galaxies may be driven by rare, highly energetic stellar explosions, with HSCJ1631+4426 and SDSSJ0811+4730 providing valuable local environments for constraining nucleosynthetic pathways that likely operated in the early Universe. The spatially resolved KCWI data further offer the opportunity for future full spectral fitting to characterize stellar populations, kinematics, and interstellar medium (ISM) conditions across these systems.

ACKNOWLEDGEMENTS

AM is grateful for the support through an Australian Government Research Training Program Scholarship (RTPS). This research was also supported by the Australian Research Council Centre of Excellence for All Sky Astrophysics in 3 Dimensions (ASTRO 3D), through project number CE170100013. TN and KG acknowledge support from Australian Research Council Laureate Fellowship FL180100060. TN acknowledges support from Australian Research Council Discovery Project DP230103161. SMS acknowledges funding from the Australian Research Council (DE220100003). JB acknowledges support by FCT through national funds (UID/FIS/04434/2013) and by FEDER through COMPETE2020 (POCI-01-0145-FEDER-007672). YI was supported by JSPS KAKENHI Grant No. 24KJ0202. CK acknowledges funding from the UK Science and Technology Facilities Council through grant ST/Y001443/1. MVM was supported by the National Science Foundation via AAG grant 2205519. We thank the staff located at the W. M. Keck Observatory for their assistance during the observations. The observations reported here were obtained under Keck programme 2022A_W226.

Some of the data presented herein were obtained at Keck Observatory, which is a private 501(c)3 non-profit organization operated as a scientific partnership among the California Institute of Technology, the University of California, and the National Aeronautics and Space Administration. The Observatory was made possible by the generous financial support of the W. M. Keck Foundation. The authors wish to recognize and acknowledge the very significant cultural role and reverence that the summit of Maunakea has always had within the Native Hawaiian community. We are most fortunate to have the opportunity to conduct observations from this mountain.

Facility: Keck:II (KCWI)

DATA AVAILABILITY

The data underlying this article will be shared on reasonable request to the corresponding author.

Downloaded from academic.oup.com/mnras/article/552/3/stag1816/8834024 by :: user on 05 November 2026

REFERENCES

Asplund M., Grevesse N., Sauval A. J., Scott P., 2009, ARA&A, 47, 481
Asplund M., Amarsi A. M., Grevesse N., 2021, A&A, 653, A141
Bacon R. et al., 2023, A&A, 670, A4
Badnell N. R., Ballance C. P., 2014, ApJ, 785, 99
Bensby T., Feltzing S., 2006, MNRAS, 367, 1181
Bensby T., Feltzing S., Oey M. S., 2014, A&A, 562, A71
Campbell A., Terlevich R., Melnick J., 1986, MNRAS, 223, 811
Cardelli J. A., Clayton G. C., Mathis J. S., 1989, ApJ, 345, 245
Cayrel R. et al., 2004, A&A, 416, 1117
Chabrier G., 2003, PASP, 115, 763
Cresci G., Mannucci F., Maiolino R., Marconi A., Gnerucci A., Magrini L., 2010, Nature, 467, 811
Cullen F. et al., 2019, MNRAS, 487, 2038
Deb N. C., Hibbert A., 2009, At. Data Nucl. Data Tables, 95, 184
Edvardsson B., Andersen J., Gustafsson B., Lambert D. L., Nissen P. E., Tomkin J., 1993, A&A, 275, 101
Garnett D. R., 1992, AJ, 103, 1330
Gratton R. G., Carretta E., Claudi R., Lucatello S., Barbieri M., 2003, A&A, 404, 187
Hawcroft C. et al., 2025, ApJS, 280, 5
Heger A., Woosley S. E., 2002, ApJ, 567, 532
Isobe Y. et al., 2022, ApJ, 925, 111
Isobe Y. et al., 2026, MNRAS, 547, stag123
Izotov Y. I., Stasińska G., Meynet G., Guseva N. G., Thuan T. X., 2006, A&A, 448, 955
Izotov Y. I., Thuan T. X., Guseva N. G., 2012, A&A, 546, A122
Izotov Y. I., Thuan T. X., Guseva N. G., Liss S. E., 2018, MNRAS, 473, 1956
Ji X. et al., 2024, MNRAS, 535, 881
Johansson S., Zethson T., Hartman H., Ekberg J. O., Ishibashi K., Davidson K., Gull T., 2000, A&A, 361, 977
Kashino D. et al., 2022, ApJ, 925, 82
Kashiwagi Y. et al., 2021, PASJ, 73, 1631
Kobayashi C., Karakas A. I., Umeda H., 2011, MNRAS, 414, 3231
Kobayashi C., Karakas A. I., Lugaro M., 2020, ApJ, 900, 179
Kojima T. et al., 2020, ApJ, 898, 142
Kojima T. et al., 2021, ApJ, 913, 22
Luridiana V., Morisset C., Shaw R. A., 2015, A&A, 573, A42
Maoz D., Mannucci F., Nelemans G., 2014, ARA&A, 52, 107
Mendoza C., Méndez-Delgado J. E., Bautista M., García-Rojas J., Morisset C., 2023, Atoms, 11, 63
Méndez-Delgado J. E. et al., 2024, A&A, 690, A248
Modjaz M. et al., 2020, ApJ, 892, 153
Myszka A. et al., 2025, MNRAS, 540, 919
Nahar S. N., Pradhan A. K., 1996, A&AS, 119, 509
Nakane M. et al., 2024, ApJ, 976, 122
Nakane M. et al., 2025, ApJ, 994, 65
Newville M., Stensitzki T., Allen D. B., Ingargiola A., 2014, LMFIT: non-linear least-square minimization and curve-fitting for Python, Zenodo, doi:10.5281/zenodo.11813
Nielsen N. M., Kacprzak G. G., Sameer, Murphy M. T., Nateghi H., Charlton J. C., Churchill C. W., 2022, MNRAS, 514, 6074
Nomoto K., Kobayashi C., Tominaga N., 2013, ARA&A, 51, 457
Osterbrock D. E., 1989, Astrophysics of Gaseous Nebulae and Active Galactic Nuclei. University Science Books, Cambridge, Massachusetts, United States
Quinet P., 1996, A&AS, 116, 573
Rakavy G., Shaviv G., 1967, ApJ, 148, 803
Reddy B. E., Tomkin J., Lambert D. L., Allende Prieto C., 2003, MNRAS, 340, 304
Robitaille T., Rice T., Beaumont C., Ginsburg A., MacDonald B., Rosolowsky E., 2019, Astrophysics Source Code Library, record ascl:1907.016
Rodríguez M., Rubin R. H., 2005, ApJ, 626, 900
Stanton T. M. et al., 2024, MNRAS, 532, 3102
Steidel C. C., Strom A. L., Pettini M., Rudie G. C., Reddy N. A., Trainor R. F., 2016, ApJ, 826, 159
Suzuki A., Maeda K., 2018, ApJ, 852, 101
Tacchella S. et al., 2025, MNRAS, 540, 851
Thuan T. X., Guseva N. G., Izotov Y. I., 2022, MNRAS, 516, L81
Umeda H., Nomoto K., 2008, ApJ, 673, 1014
Watanabe K. et al., 2024, ApJ, 962, 50
Xing Q.-F., Zhao G., Aoki W., Honda S., Li H.-N., Ishigaki M. N., Matsuno T., 2019, Nat. Astron., 3, 631

This paper has been typeset from a TEX/LATEX file prepared by the author.

Downloaded from academic.oup.com/mnras/article/552/3/stag1816/8834024 by :: user on 05 November 2026

© The Author(s) 2026.
Published by Oxford University Press on behalf of Royal Astronomical Society. This is an Open Access article distributed under the terms of the Creative Commons Attribution License (https://creativecommons.org/licenses/by/4.0/), which permits unrestricted reuse, distribution, and reproduction in any medium, provided the original work is properly cited.